Letter

Fractal patterns in the parameter space of a bistable Duffing oscillator

Md Nahid Hasan⊙, Taylor E. Greenwood⊙, Robert G. Parker⊙, Yong Lin Kong⊙,[*] and Pai Wang⊙[†]

Department of Mechanical Engineering, University of Utah, Salt Lake City, Utah 84112, USA

We study the dissipative bistable Duffing oscillator with equal energy wells and observe fractal patterns in the parameter space of driving frequency, forcing amplitude, and damping ratio. Our numerical investigation reveals the Hausdorff fractal dimension of the boundaries that separate the oscillator's intrawell and interwell behaviors. Furthermore, we categorize the interwell behaviors as three steady-state types: switching, reverting, and vacillating. While fractal patterns in the phase space are well known and heavily studied, our results point to another research direction about fractal patterns in the parameter space. Another implication of this study is that the vibration of a continuous bistable system modeled using a single-mode approximation also manifests fractal patterns in the parameter space. In addition, our findings can guide the design of next-generation bistable and multistable mechanical metamaterials.

Introduction. The dissipative bistable Duffing oscillator is a well-known dynamical system with applications in many fields, such as shape morphing [1], energy harvesting [2], soft robotics [3], microelectromechanical system (MEMS) devices [4], energy absorption [5], and drug delivery [6]. In addition, with recent advances in the multistable metamaterial [7,8], and advanced functional systems [9], bistable system dynamics can be introduced as a mechanism for folding and reprogramming [10]. Equation (1) represents the general dimensionless form of the bistable Duffing equation with symmetric double potential wells around two stable equilibria at $u_{-1} = -1$ and $u_{+1} = +1$, which are separated by a "hilltop" unstable equilibrium at $u_0 = 0$ (see Supplemental Material [11] for the detailed derivation):

$$\ddot{u} + \gamma \dot{u} - u + \mu u^3 = G\cos(\Omega\tau). \tag{1}$$

The frequency response curve [12] is a standard tool to describe the bistable system dynamics by solving Eq. (1) in the frequency domain, but it does not provide a complete picture. Instead, analyses on the potential well escape provide advantages to investigate the overall dynamics [13–17]. For example, energy criteria [18–23], forcing phase [24], and velocity conditions [25] offer valuable information. However, due to the uncertainty of the initial conditions [26,27] and fractal basin boundaries in the phase space [25,28–37], most recent studies are unable to conclusively determine in which potential well (right or left) the system will reside after the escape. In addition, system parameters such as frequency (Ω), forcing amplitude (G), and damping ratio (γ) also influence the system's final state. In a previous publication, Moon analyzed the parameter plane of forcing amplitude and frequency [38]. They identified a fractal boundary between

a bistable Duffing oscillator's intrawell and interwell behaviors. Although a fractal dimension of 1.26 was calculated from limited experimental data, the statistical complexity of the fractal boundary requires further data analysis. Furthermore, the study on the single-well Duffing system also shows fractal-like patterns of "Arnold's tongues" [39] in the parameter plane, which motivates us to investigate further the fractal nature of the region boundaries of the double-well bistable Duffing oscillator. Soskin *et al.* investigated the criterion of reaching the coordinate of a saddle in Hamiltonian systems and found fractal-like patterns in the parameter space. However, the fractal dimension of the parameter space was not calculated in their studies [40,41]. In addition, Mathias *et al.* observed the presence of fractal structures in the parameter space of a nontwist area-preserving map [42].

In this Letter, we propose numerical criteria addressing the oscillator's categories of behavior between potential wells. To avoid the well-known sensitivity due to the initial condition, we fix the initial conditions at $(u, \dot{u}) = (-1, 0)$ in all simulations. Furthermore, we seek to conduct rigorous numerical simulations to categorize different system behaviors and calculate accurate fractal dimensions in the parameter space. We first reexamine the frequency response curve and the parameter space of the bistable Duffing oscillator. Importantly, our numerical investigation reveals that the single-degree-of-freedom (SDOF) model based on a single-vibration-mode assumption exhibits the fractal pattern very well. Next, we categorize the different steady-state response behaviors inside the parameter space. Finally, we calculate the fractal dimensions of the boundaries that separate the interwell and intrawell behaviors in the parameter space. The fractal dimension reveals the statistical complexity of the parameter space of the bistable Duffing system. Our results indicate that interwell behavior, traditionally defined as chaotic behavior, can be understood and has potential applications in shape morphing.

Frequency response curve and its limitations. We start with time-domain simulations using the fourth-order Runge-Kutta
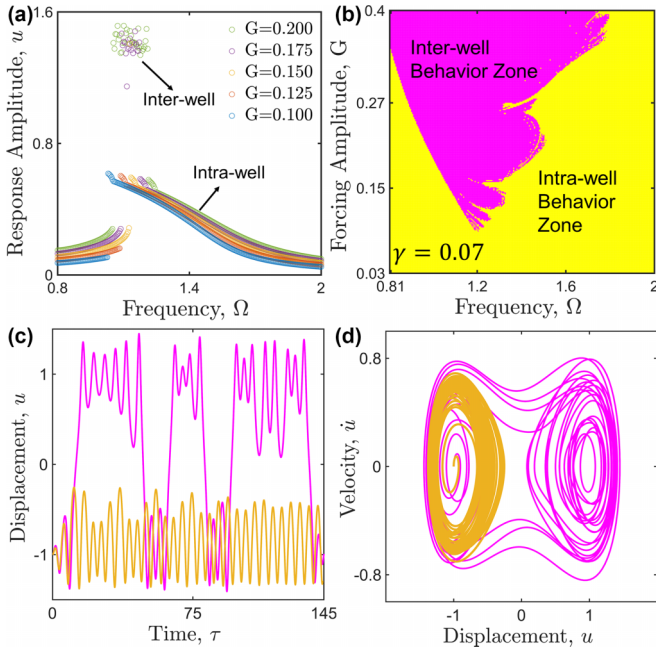
---

[*]yong.kong@utah.edu
[†]pai.wang@utah.edu

FIG. 1. (a) Five frequency response curves across values of forcing amplitude G and for $\gamma = 0.07$. (b) Forcing amplitude-frequency (G vs Ω) parameter space where magenta and yellow zones represent interwell and intrawell behavior regions, respectively. (c), (d) Time-domain and the phase-space responses of interwell (magenta) behavior with parameters $(G, \Omega) = (0.175, 1.13291)$ and intrawell (yellow) behavior with parameters $(G, \Omega) = (0.150, 1.30506)$, respectively, for $\gamma = 0.07$.

scheme over a broad range of (G, Ω) for a constant damping ratio of $\gamma = 0.07$ to discern the interwell and intrawell responses. In Fig. 1(a), we sweep the forcing frequency Ω in the range of $0.80 \leqslant \Omega \leqslant 2.0$ at a step size of 0.0047. We also sweep the forcing amplitude G in the range of $0.100 \leqslant G \leqslant 0.200$ at a step size of 0.025. In each simulation, we solve Eq. (1) to obtain the time response of 500 forcing cycles. Then we capture the average peak-to-peak steady-state amplitude of the last 50 periods of the time response. In all cases, we start with the initial conditions of $(u, \dot{u}) = (-1, 0)$. First, we examine the frequency response curve in Fig. 1(a). It shows multiple solutions, both interwell and intrawell, coexisting near $\Omega = 1.0$. This is the root cause of the hysteresis jump phenomena [18,19]. Consequently, the standard frequency response curve cannot provide enough information about potential-well escape criteria.

We then consider the parameter space of forcing amplitude and driving frequency (G and Ω) and use a 256×256 grid to plot the results in Fig. 1(b). We obtain the time history for 500 periods in each simulation. If the response amplitude, which begins at $u_{-1} = -1$ based on the initial condition, exceeds the hilltop equilibrium at $u_0 = 0$, then the response exhibits the interwell behavior. Alternatively, if the response amplitude does not exceed the unstable equilibrium at u_0 in all 500 periods, we recognize this response as the intrawell behavior. The two different parameter regions are illustrated in Fig. 1(b). As examples, Figs. 1(c) and 1(d) show the time and phase-space responses of the interwell (magenta

curves) and intrawell (yellow curves) behaviors. We observe that the boundary between the interwell and intrawell zones in Fig. 1(b) takes an intricate shape. Near the boundary, the oscillator's behavior is highly sensitive to a subtle change in the amplitude and frequency of the excitation. This shows that the single-mode SDOF model can capture fractal patterns in the parameter space of a bistable system, contrary to the argument that higher-order vibration modes with more degrees of freedom are required [38].

Categories of steady-state behaviors in the parameter space. Figure 1 shows two behaviors: intrawell oscillation near one stable equilibrium, and interwell between two stable equilibria [43]. However, a thorough investigation of the dynamics of a double-well potential system with harmonic excitation uncovers opportunities for unique applications, as it exhibits four possible types of behavior: (i) Switching: interwell behavior where the oscillation begins in one potential well, and after the transient stage, reaches its steady state in the other potential well; (ii) reverting: interwell behavior where the oscillation begins in one potential well, reaches the other potential well during the transient stage, and eventually returns to its original potential well in the steady state; (iii) vacillating: interwell behavior where the oscillation keeps moving between the two wells, and it never settles into either one; and (iv) intrawell: steady-state oscillation in one potential well only.

To quantitatively distinguish these categories of behavior using numerical results from time-domain simulations, we first check whether the system displacement amplitude, which begins at u_{-1} based on the initial condition, exceeds the hilltop equilibrium at u_0. Then, we recognize the last 50 cycles as the steady-state output of the total of 500 cycles in the simulations. Based on this numerical assumption, we define $\xi_{max} = \max[u(t)|t \in \{\text{last 50 cycles}\}]$ and $\xi_{min} = \min[u(t)|t \in \{\text{last 50 cycles}\}]$. As illustrated in Fig. 2(a) (note that a much smaller number of cycles are shown here for illustration purposes), if $\xi_{max} > 0$ and $\xi_{min} > 0$, we categorize this behavior as switching. In Fig. 2(b), the phase-space plot of the same simulation illustrates the growth of the oscillator's limit cycle oscillations (LCOs) [44] from u_{-1}, and it eventually reaches a steady-state trajectory near u_{+1}. This picture resembles the stable LCOs in many studies [24,44,45]. Thus, up to the numerical precision, we can conclude that the oscillator stabilizes in the second stable state [45] and categorize this as the switching behavior. In Fig. 2(c), the oscillator switches from the u_{-1} potential well to the u_{+1} one during the transient stage. For the steady state, we observe $\xi_{max} < 0$ and $\xi_{min} < 0$, meaning it reverts back to its initial well at u_{-1} in the end. We categorize this behavior as reverting. Correspondingly, we see a stable limit cycle around the stable equilibrium at u_{-1} in Fig. 2(d). Next, in Figs. 2(e) and 2(g), the oscillator's interwell behavior exhibits persistent shifting between u_{-1} to u_{+1}. The observation of $\xi_{max} > 0$ and $\xi_{min} < 0$ in the steady state implies that it continues to oscillate between both potential wells without settling into either one, so we can categorize these behaviors as vacillating. We also analyze the phase-space behavior to distinguish between periodic and aperiodic vacillating behaviors. Figure 2(f) illustrates periodic vacillating where the phase-space trajectory follows a high-energy orbit motion outside of
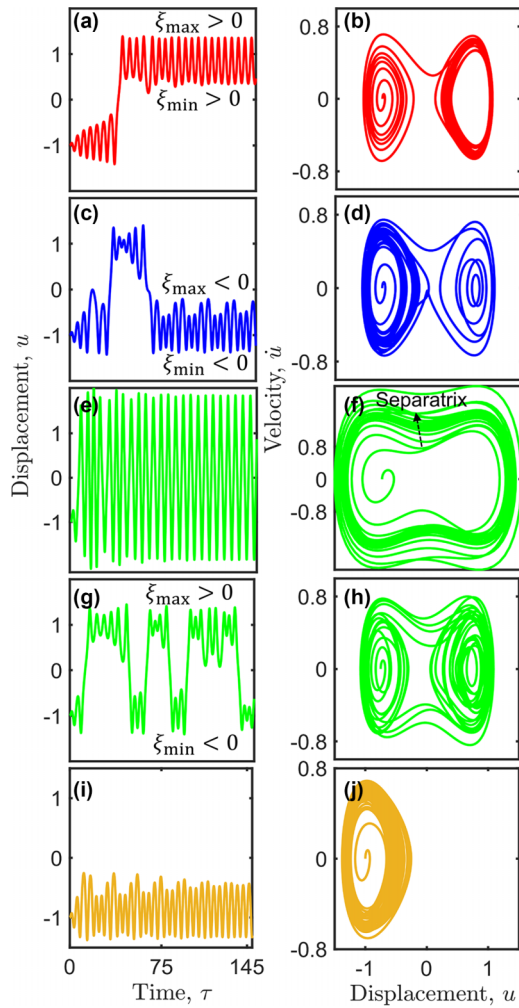
FIG. 2. Categories of time domain and phase space of behaviors with damping ratio $\gamma = 0.07$: (a), (b) Switching behavior with parameters $(G, \Omega) = (0.100, 1.17595)$. (c), (d) Reverting behavior with parameters $(G, \Omega) = (0.125, 1.209412)$. (e), (f) Periodic vacillating behavior with parameters $(G, \Omega) = (0.400, 1.10294)$. (g), (h) Aperiodic vacillating behavior with parameters $(G, \Omega) = (0.175, 1.13291)$. (i), (j) Intrawell behavior with parameters $(G, \Omega) = (0.150, 1.30506)$.

the separatrix [44], while Fig. 2(h) shows low-energy orbits around either one or two potential wells inside the separatrix. Finally, Fig. 2(i) displays the intrawell behavior, which remains in the vicinity of the stable equilibrium at u_{-1} without reaching the unstable equilibrium at u_0. Figure 2(j) shows the stable limit cycle around u_{-1} corresponding to the intrawell confinement.

Fractal patterns in the parameter space. Using the four categories of behaviors described in the last section, we update our understanding of the parameter space of Fig. 1(b). For each set of (G, Ω), we run time-domain simulations in the parameter ranges of $0.80 \leqslant \Omega \leqslant 1.8$ and $0.03 \leqslant G \leqslant 0.30$ with different damping ratios. Figures 3(a)–3(f) show the results for $\gamma = 0.001, 0.07, 0.15, 0.25,$ and 0.30, respectively (see Supplemental Material [11] for more results with other damping ratios). We categorize the numerical steady state of each simulation either as switching, reverting, vacillating, or

intrawell behavior. We represent them as red, blue, green, and yellow data points in Fig. 3, respectively. The minimally required forcing amplitude $G_{\min}$ for interwell behavior rises as γ increases. For example, Fig. 3(a) indicates the minimum amplitude required for interwell behavior is $G = 0.04$. In contrast, in Figs. 3(b) and 3(c), it is about $G = 0.09$. In all cases, we see the well-known V-shaped "Arnold's tongue," whose bottom tip represents $G_{\min}$ for vacillating behavior. As damping increases, the tip of Arnold's tongue moved up and left towards $\Omega = 1$. Figure 3(a), in particular, shows that the vacillating behavior dominates among all interwell behaviors in the low damping limit. This means that low dissipation increases the likelihood of vacillating behavior.

In general, the results in Fig. 3 suggest that, compared to the quasistatic actuation [47], utilizing harmonic excitation can significantly reduce the forcing amplitude necessary to switch between stable states. For the given system under quasistatic loading, a dimensionless force of 0.38 is required for switching between stable states (see Supplemental Material [11]). In contrast, as shown in Fig. 3(a), interwell behavior can be achieved with a much lower dimensionless actuation forcing amplitude of $G_{\min} = 0.04$, which is one order of magnitude lower than the required quasistatic actuation force. These results highlight the importance of optimizing the (G, Ω, γ) parameters to achieve interwell behavior in the system. Moreover, incorporating feedback control strategies [10] can further enhance the controlled switching between stable states, resulting in a more efficient actuation mechanism than the quasistatic actuation.

To gain a better understanding of the intricacy of parameter space, we focus on the region enclosed by the black frame in Fig. 3(b). A higher-resolution picture of the same region is plotted as Fig. 3(c). It shows feather-shaped self-similar patterns and strongly suggests the existence of fractals in the parameter space of the bistable Duffing oscillator. Motivated by the fractal pattern in the forcing amplitude-frequency (G vs Ω) parameter plane, we also investigate the damping ratio-forcing frequency (γ vs Ω) parameter plane. Figure 4 shows the results in the parameter range $0.80 \leqslant \Omega \leqslant 1.8$ and $0.00 \leqslant \gamma \leqslant 0.35$ for $G = 0.1, 0.125, 0.15, 0.2, 0.225,$ and 0.25, respectively (see Supplemental Material [11] for more results with other forcing amplitudes). The patterns look similar to those shown in Fig. 3, but they have flipped upside down with the top tip indicating the maximally allowed damping for interwell behavior. As Fig. 3, with increasing forcing amplitude G, the Arnold's tongue tip moves up and left towards $\Omega = 1$. Feather-shaped fractal patterns with self-similarity also appear. The results show that higher forcing amplitude and lower dissipation lead to a higher likelihood of vacillating behavior in the steady state.

Fractal dimension of boundaries in the parameter space. After examining the motion categories presented in Fig. 2, we observe the existence of self-similar fractal patterns in Figs. 3 and 4. Now, we aim to calculate the Hausdorff fractal dimension [48] F_D of the parameter-space boundaries between the interwell and intrawell behaviors. This aims at deepening our understanding of the statistical complexity of the fractal boundaries. To accomplish this, we simplify the parameter space by considering only two categories instead of four: interwell and intrawell behavior, as shown in Figs. 5(a) and
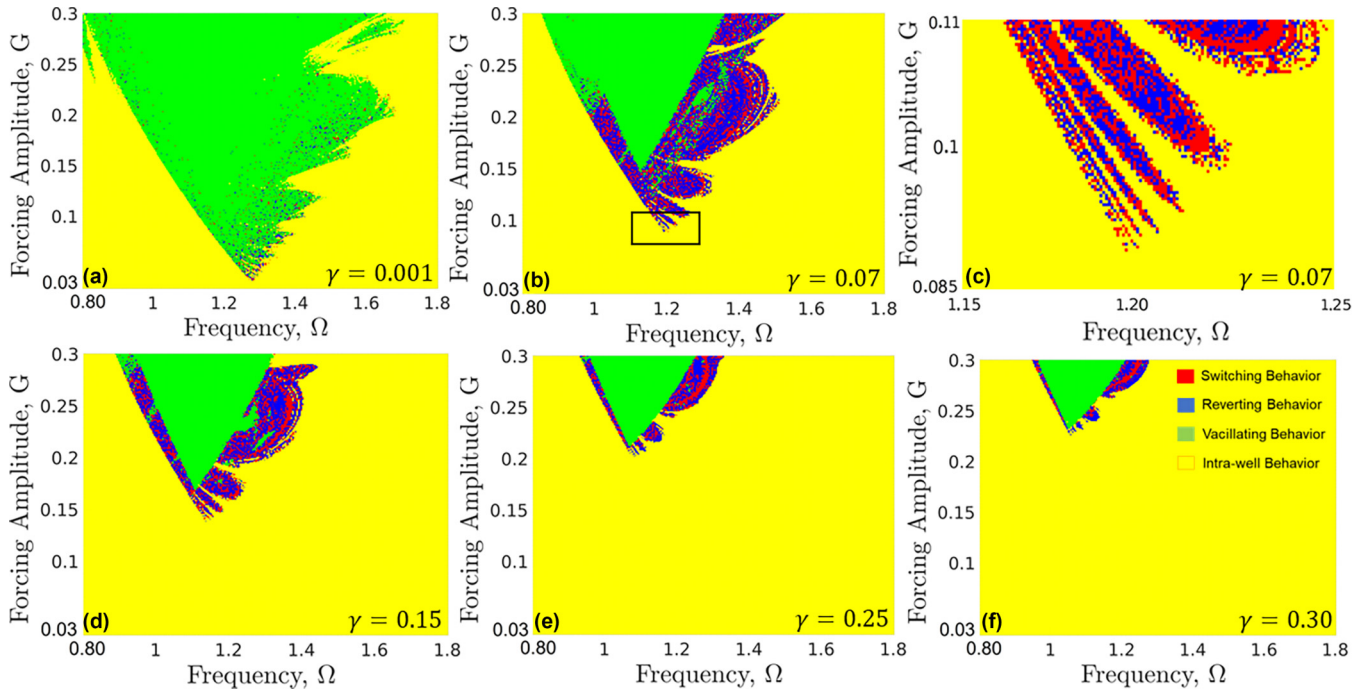
FIG. 3. Forcing amplitude-frequency (G vs Ω) parameter space (sampled over a uniform grid of 256×256) with (a) damping ratio $\gamma = 0.001$ and (b) $\gamma = 0.07$. (c) Zoom-in of the black-framed portion of (b), which shows the fractal nature. (d) $\gamma = 0.15$. (e) $\gamma = 0.25$. (f) $\gamma = 0.30$.

5(c). This is motivated by the fact that all types of interwell motions can lead to switching between stable states at least once.

As illustrated in Figs. 5(b) and 5(d), we implement the box-counting algorithm [49] to calculate the Hausdorff fractal

dimension of extracted boundary curves in each parameter-space plot. We use square-shaped boxes of variable size ϵ to cover the boundary curves [e.g., black lines in Figs. 5(b) and 5(d)], and count the total number of boxes, $N(\epsilon)$, needed to cover all boundaries. As $\epsilon \to 0$, $N(\epsilon) \to \infty$, and we obtain
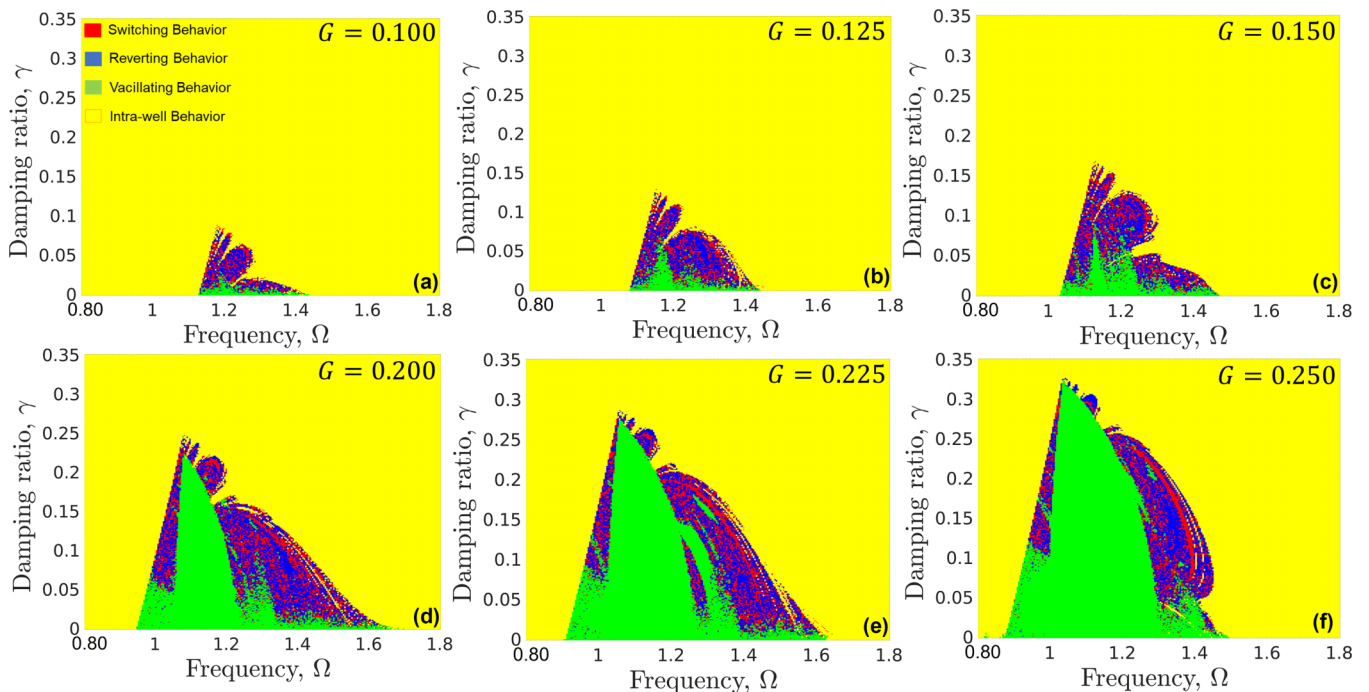

FIG. 4. Damping ratio-forcing frequency (γ vs Ω) parameter space (sampled over a uniform grid of 256×256) with (a) forcing amplitude $G = 0.100$, (b) $G = 0.125$, (c) $G = 0.150$, (d) $G = 0.200$, (e) $G = 0.225$, and (f) $G = 0.250$.
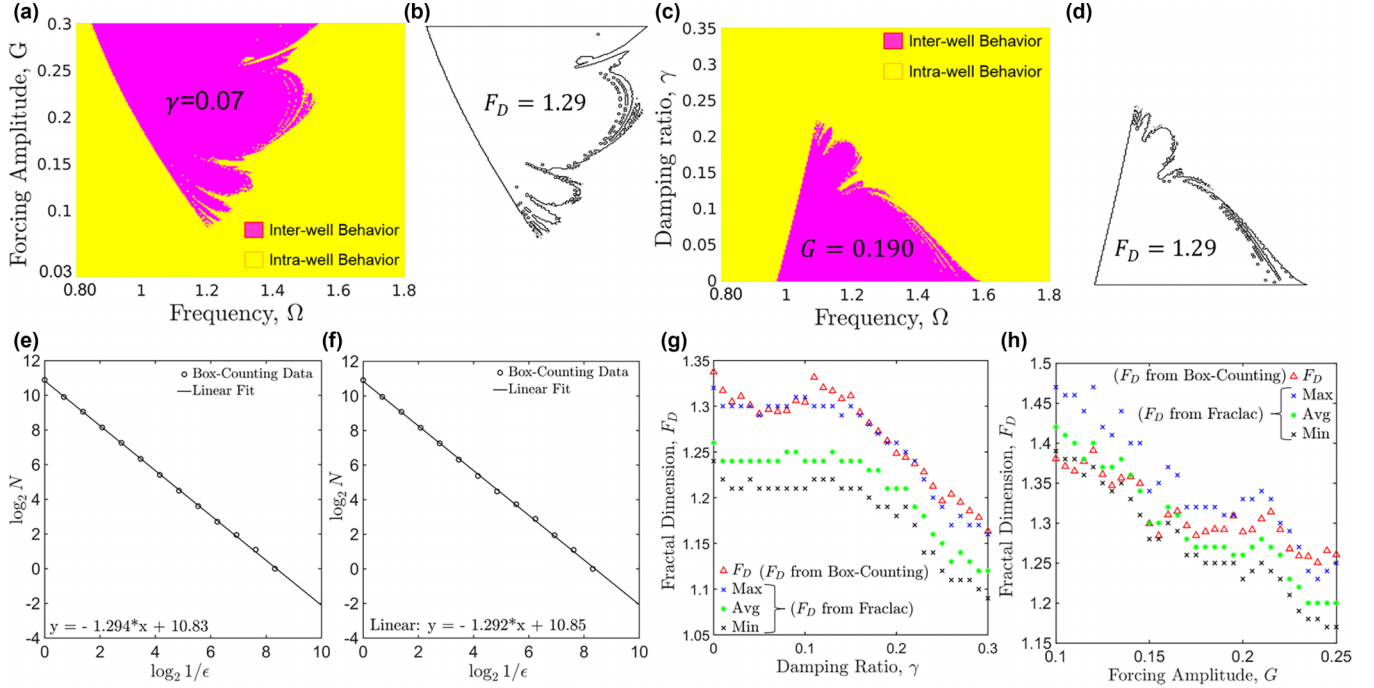
FIG. 5. Fractal dimension of the boundaries in forcing amplitude-frequency (G vs Ω) and damping ratio-forcing frequency (γ vs Ω) parameter space: (a) An example with the damping ratio of $\gamma = 0.07$. (b) Fractal boundary between interwell and intrawell regions. (c) An example with the forcing amplitude of $G = 0.190$. (d) Fractal boundary between interwell and intrawell regions. (e) and (f) show the linear regression of the box-counting algorithm data for (b) and (d) using the least-squares method to calculate the Hausdorff fractal dimension. (g) illustrates the Hausdorff fractal dimension of the boundaries in (G vs Ω) parameter space as the damping ratio increases from $0.001 \leqslant \gamma \leqslant 0.30$ with a step size of 0.01. (h) illustrates the Hausdorff fractal dimension of the boundaries in (γ vs Ω) parameter space as the forcing amplitude increases from $0.10 \leqslant G \leqslant 0.25$ with a step size of 0.005. The red ($\triangle$) markers show the box-counting algorithm implementation's F_{D} results. The blue ($\times$), green ($*$), and black ($\times$) markers show the maximum, average, and minimum F_{D} results from the image processing software FRACLAC/IMAGEJ [46].

F_{D} as

$$F_{\mathrm{D}} = \left| \lim_{\epsilon \to 0} \left[\log(N)/\log\left(\frac{1}{\epsilon}\right) \right] \right|. \qquad (2)$$

Finally, we use the least-squares method to perform linear regression on the $\log(N)$ vs $\log(\frac{1}{\epsilon})$ plot to determine F_{D}. For example, the linear regressions shown in Figs. 5(e) and 5(f) generate $F_{\mathrm{D}} = 1.29$ and $F_{\mathrm{D}} = 1.29$ for the parameter-space boundaries shown in Figs. 5(b) and 5(d), respectively. To verify our implementation, we also use the software FRACLAC/IMAGEJ [46] developed by the National Institutes of Health (NIH). It determines the fractal dimensions of Figs. 5(b) and 5(d) as 1.2813 and 1.27, respectively, which has a close agreement with our numerical predictions of F_{D} from Figs. 5(e) and 5(f).

It is worth noting that the level of magnification is a crucial factor when using the box-counting algorithm to calculate the fractal dimension, as highlighted in previous studies [50,51]. The nature of fractal patterns, in fact, entails that they can always give finer details at any smaller scale. We observe that, as we increase the level of magnification (i.e., higher resolution), the fractal dimension resulting from box counting approaches a plateau (see Supplemental Material [11]). This plateau indicates that the fractal dimension has reached the "mesh convergence," where "mesh" here refers to the numerical resolution in the parameter space. In other words, this convergence supports that the fractal dimension

in the parameter space remains consistent as we further zoom in.

Following the above procedure, we calculate the fractal dimensions of boundaries in 31 forcing amplitude-frequency plots and 31 damping ratio-forcing frequency plots of the parameter space (see Supplemental Material [11]) for $0.001 \leqslant \gamma \leqslant 0.30$ and $0.10 \leqslant G \leqslant 0.25$, respectively. Using FRACLAC/IMAGEJ [46], we also calculate the average, maximum, and minimum fractal dimensions in all cases. We summarize all results in Fig. 5(g) for different damping ratios and Fig. 5(h) for different forcing amplitudes, respectively. The Hausdorff fractal dimension plotted here characterizes the boundaries between interwell and intrawell motions. We observe a downward trend with an increasing damping ratio or forcing amplitude. This indicates that higher damping and higher forcing amplitude can reduce the complexity of the dynamical behavior of the bistable Duffing oscillator.

Conclusion. We show that four system behaviors (switching, reverting, vacillating, and intrawell) exist as different regions in the parameter space of a dissipative bistable Duffing oscillator. Our numerical results reveal the fractal nature of the boundaries between the interwell and intrawell regions. The box-counting algorithm leads to characterizing the Hausdorff fractal dimension of these boundaries. This study exclusively focuses on the fractal patterns in the parameter space, which are often neglected compared to those in the phase space.

[1] Y. Cao, M. Derakhshani, Y. Fang, G. Huang, and C. Cao, Bistable structures for advanced functional systems, Adv. Funct. Mater. **31**, 2106231 (2021).

[2] R. L. Harne and K. Wang, A review of the recent research on vibration energy harvesting via bistable systems, Smart Mater. Struct. **22**, 023001 (2013).

[3] Y. Chi, Y. Li, Y. Zhao, Y. Hong, Y. Tang, and J. Yin, Bistable and multistable actuators for soft robots: Structures, materials, and functionalities, Adv. Mater. **34**, 2110384 (2022).

[4] J. Qiu, J. H. Lang, and A. H. Slocum, A curved-beam bistable mechanism, J. Microelectromech. Syst. **13**, 137 (2004).

[5] S. Sun, N. An, G. Wang, M. Li, and J. Zhou, Snap-back induced hysteresis in an elastic mechanical metamaterial under tension, Appl. Phys. Lett. **115**, 091901 (2019).

[6] B. Wagner, H. Quenzer, S. Hoerschelmann, T. Lisec, and M. Juerss, Micromachined bistable valves for implantable drug delivery systems, in *Proceedings of 18th Annual International Conference of the IEEE Engineering in Medicine and Biology Society* (IEEE, New York, 1996), Vol. 1, pp. 254–255.

[7] M. N. Hasan, T. Greenwood, Y. Lin Kong, and P. Wang, Optimization of the small-amplitude dynamic triggering mechanism of bi-stable metamaterials, Bull. Am. Phys. Soc., https://meetings.aps.org/Meeting/MAR23/Session/D09.13 (2023).

[8] T. Greenwood, M. N. Hasan, P. Wang, and Y. L. Kong, Advanced manufacturing of multi-stable metamaterials, Bull. Am. Phys. Soc., https://meetings.aps.org/Meeting/MAR23/Session/S05.11 (2023).

[9] Y. Tang, M. Li, T. Wang, X. Dong, W. Hu, and M. Sitti, Wireless miniature magnetic phase-change soft actuators, Adv. Mater. **34**, 2204185 (2022).

[10] S. Sadeghi and S. Li, Dynamic folding of origami by exploiting asymmetric bi-stability, Extreme Mech. Lett. **40**, 100958 (2020).

[11] See Supplemental Material at http://link.aps.org/supplemental/10.1103/PhysRevE.108.L022201 for additional results, detailed derivations, and calculation procedures.

[12] W. Wawrzynski, Duffing-type oscillator under harmonic excitation with a variable value of excitation amplitude and time-dependent external disturbances, Sci. Rep. **11**, 2889 (2021).

[13] W. Szemplińska-Stupnicka, The analytical predictive criteria for chaos and escape in nonlinear oscillators: A survey, Nonlinear Dyn. **7**, 129 (1995).

[14] J. M. T. Thompson, Chaotic phenomena triggering the escape from a potential well, Proc. R. Soc. London, Ser. A **421**, 195 (1989).

[15] A. Lansbury and J. Thompson, Incursive fractals: A robust mechanism of basin erosion preceding the optimal escape from a potential well, Phys. Lett. A **150**, 355 (1990).

[16] J. M. T. Thompson and M. S. Soliman, Indeterminate jumps to resonance from a tangled saddle-node bifurcation, Proc. R. Soc. London, Ser. A **432**, 101 (1991).

[17] H. Stewart, J. Thompson, Y. Ueda, and A. Lansbury, Optimal escape from potential wells-patterns of regular and chaotic bifurcation, Physica D **85**, 259 (1995).

[18] L. Virgin and B. Erickson, A new approach to the overturning stability of floating structures, Ocean Eng. **21**, 67 (1994).

[19] J. Gottwald, L. Virgin, and E. Dowell, Routes to escape from an energy well, J. Sound Vib. **187**, 133 (1995).

[20] L. N. Virgin, R. H. Plaut, and C.-C. Cheng, Prediction of escape from a potential well under harmonic excitation, Int. J. Non-Linear Mech. **27**, 357 (1992).

[21] J. Gottwald, L. Virgin, and E. Dowell, Experimental mimicry of Duffing's equation, J. Sound Vib. **158**, 447 (1992).

[22] L. N. Virgin and L. A. Cartee, A note on the escape from a potential well, Int. J. Non-Linear Mech. **26**, 449 (1991).

[23] L. N. Virgin, *Introduction to Experimental Nonlinear Dynamics: A Case Study in Mechanical Vibration* (Cambridge University Press, Cambridge, UK, 2000).

[24] J. P. Udani and A. F. Arrieta, Efficient potential well escape for bi-stable duffing oscillators, Nonlinear Dyn. **92**, 1045 (2018).

[25] F. C. Moon, Experiments on chaotic motion of a forced nonlinear oscillator: Strange attractors, J. Appl. Mech. **47**, 638 (1980).

[26] C. Grebogi, S. W. McDonald, E. Ott, and J. A. Yorke, Final state sensitivity: An obstruction to predictability, Phys. Lett. A **99**, 415 (1983).

[27] A. Puy, A. Daza, A. Wagemakers, and M. A. Sanjuán, A test for fractal boundaries based on the basin entropy, Commun. Nonlinear Sci. Numer. Simulat. **95**, 105588 (2021).

[28] F. C. Moon and G.-X. Li, Fractal Basin Boundaries and Homoclinic Orbits for Periodic Motion in a Two-Well Potential, Phys. Rev. Lett. **55**, 1439 (1985).

[29] H. E. Nusse, J. A. Yorke, and E. J. Kostelich, Basins of attraction, in *Dynamics: Numerical Explorations* (Springer, Berlin, 1994), pp. 269–314.

[30] J. Thompson, S. Bishop, and L. Leung, Fractal basins and chaotic bifurcations prior to escape from a potential well, Phys. Lett. A **121**, 116 (1987).

[31] F. Moon and P. J. Holmes, A magnetoelastic strange attractor, J. Sound Vib. **65**, 275 (1979).

[32] P. Holmes, A nonlinear oscillator with a strange attractor, Philos. Trans. R. Soc. London, Ser. A **292**, 419 (1979).

[33] C. Grebogi, E. Ott, and J. A. Yorke, Chaos, strange attractors, and fractal basin boundaries in nonlinear dynamics, Science **238**, 632 (1987).

[34] M. Tarnopolski, On the fractal dimension of the Duffing attractor, Rom. Rep. Phys. **66**, 907 (2014).

[35] F. C. Moon and G.-X. Li, The fractal dimension of the two-well potential strange attractor, Physica D **17**, 99 (1985).

[36] C. Grebogi, E. Ott, and J. A. Yorke, Chaotic Attractors in Crisis, Phys. Rev. Lett. **48**, 1507 (1982).

[37] J. Aguirre, R. L. Viana, and M. A. F. Sanjuán, Fractal structures in nonlinear dynamics, Rev. Mod. Phys. **81**, 333 (2009).

[38] F. C. Moon, Fractal Boundary for Chaos in a Two-State Mechanical Oscillator, Phys. Rev. Lett. **53**, 962 (1984).

[39] V. Paar and N. Pavin, Intermingled fractal arnold tongues, Phys. Rev. E **57**, 1544 (1998).

[40] S. M. Soskin, O. M. Yevtushenko, and R. Mannella, Drastic Facilitation of the Onset of Global Chaos, Phys. Rev. Lett. **90**, 174101 (2003).

[41] S. M. Soskin, R. Mannella, and O. M. Yevtushenko, Matching of separatrix map and resonant dynamics, with application to global chaos onset between separatrices, Phys. Rev. E **77**, 036221 (2008).

[42] A. C. Mathias, M. Mugnaine, M. S. Santos, J. D. Szezech, Jr., I. L. Caldas, and R. L. Viana, Fractal structures in the parameter space of nontwist area-preserving maps, Phys. Rev. E **100**, 052207 (2019).

[43] K.-W. Wang and R. L. Harne, *Harnessing Bistable Structural Dynamics: For Vibration Control, Energy Harvesting and Sensing* (Wiley, Hoboken, NJ, 2017).

[44] J. P. Udani and A. F. Arrieta, Sustaining high-energy orbits of bi-stable energy harvesters by attractor selection, Appl. Phys. Lett. **111**, 213901 (2017).

[45] S. H. Strogatz, *Nonlinear Dynamics and Chaos: With Applications to Physics, Biology, Chemistry, and Engineering* (CRC Press, Boca Raton, FL, 2018).

[46] U.S. National Institutes of Health (NIH), FRACLAC/IMAGEJ, https://imagej.nih.gov/ij/plugins/fraclac/FLHelp/Introduction.htm (2022).

[47] S. Shan, S. H. Kang, J. R. Raney, P. Wang, L. Fang, F. Candido, J. A. Lewis, and K. Bertoldi, Multistable architected materials for trapping elastic strain energy, Adv. Mater. **27**, 4296 (2015).

[48] F. C. Moon, *Chaotic and Fractal Dynamics: Introduction for Applied Scientists and Engineers* (Wiley, Hoboken, NJ, 2008).

[49] J. Wu, X. Jin, S. Mi, and J. Tang, An effective method to compute the box-counting dimension based on the mathematical definition and intervals, Results Eng. **6**, 100106 (2020).

[50] J. Wang, J. Ma, Q. Ao, H. Zhi, and H. Tang, Review on fractal analysis of porous metal materials, J. Chem. **2015**, 427297 (2015).

[51] H. Tang, J. Wang, J. Zhu, Q. Ao, J. Wang, B. Yang, and Y. Li, Fractal dimension of pore-structure of porous metal materials made by stainless steel powder, Powder Technol. **217**, 383 (2012).

Correction: A typographical error in the second sentence of the fourth paragraph has been fixed.